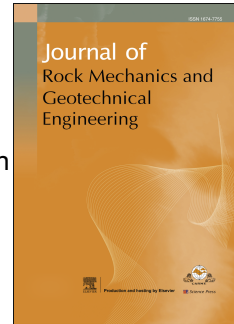


# Journal Pre-proof

Advanced 3D finite element limit analysis for assessing blowout stability in water main bursts

Jim Shiau, Tan Nguyen, Bishal Chudal



PII: S1674-7755(25)00120-9

DOI: <https://doi.org/10.1016/j.jrmge.2025.01.041>

Reference: JRMGE 1980

To appear in: *Journal of Rock Mechanics and Geotechnical Engineering*

Received Date: 14 March 2024

Revised Date: 21 January 2025

Accepted Date: 22 January 2025

Please cite this article as: Shiau J, Nguyen T, Chudal B, Advanced 3D finite element limit analysis for assessing blowout stability in water main bursts, *Journal of Rock Mechanics and Geotechnical Engineering*, <https://doi.org/10.1016/j.jrmge.2025.01.041>.

This is a PDF file of an article that has undergone enhancements after acceptance, such as the addition of a cover page and metadata, and formatting for readability, but it is not yet the definitive version of record. This version will undergo additional copyediting, typesetting and review before it is published in its final form, but we are providing this version to give early visibility of the article. Please note that, during the production process, errors may be discovered which could affect the content, and all legal disclaimers that apply to the journal pertain.

© 2025 Institute of Rock and Soil Mechanics, Chinese Academy of Sciences. Published by Elsevier B.V.

# Advanced 3D finite element limit analysis for assessing blowout stability in water main bursts

Jim Shiau<sup>a</sup>, Tan Nguyen<sup>b,\*</sup>, Bishal Chudal<sup>a</sup>

<sup>a</sup> School of Engineering, University of Southern Queensland, QLD 4350, Australia

<sup>b</sup> Smart Computing in Civil Engineering Research Group, Faculty of Civil Engineering, Ton Duc Thang University, Ho Chi Minh 700000, Vietnam

**Abstract:** The increasing occurrence of sinkholes caused by water main bursts has attracted significant research attention in recent years. This study addresses the gap in evaluating soil blowout stability resulting from water main failures by investigating the three-dimensional stability of blowouts with circular, hemispherical, and spherical openings. Advanced finite element limit analysis (FELA) combined with adaptive meshing is employed to analyze critical factors, including soil cover depth, surcharge pressure, and internal water pressure, that contribute to blowout failure. In addition, dimensionless ratios are used throughout the paper to assess the influence of these factors. Numerical findings are rigorously validated, ensuring reliability and accuracy. Practical design charts are provided to accommodate a wide range of design scenarios, offering valuable guidance for engineers. This study introduces a pioneering sinkhole simulation methodology, leading to the understanding of three-dimensional blowout stability mechanisms.

**Keywords:** Blowout stability, Cavity, Sinkhole, Finite element limit analysis (FELA)

## 1. Introduction

Urban areas, characterized by impervious structures like road pavements, parking lots, and roofs, often face challenges related to rainfall infiltration. The limited permeability of these surfaces results in stormwater runoff dominating storm sewers, leading to potential issues such as urban flooding during heavy rainfall events. To address this, innovative approaches like perforated storm sewers have been proposed to facilitate stormwater infiltration into the ground. This not only mitigates the impact of rainfall-runoff but also contributes to altering prolonged drought-like conditions.

Several recent studies have delved into different aspects of geotechnical and hydraulic engineering related to stormwater management. Cao et al. (2022) investigated the physical and numerical modeling of infiltration from drainage holes in perforated storm sewers, emphasizing the importance of understanding the dynamics of stormwater infiltration. Lan and Moore (2022) focused on a new design equation for maximum allowable mud pressure during horizontal directional drilling (HDD), highlighting the significance of stability considerations in geotechnical engineering.

Liu et al. (2021) explored the suffusion response of well-graded gravels in the roadbed of non-ballasted high-speed railways, shedding light on the mechanisms influencing soil behavior in railway construction. Qin and Moore (2022) conducted laboratory investigations into backfill erosion around rigid pipes with defective joints, addressing issues related to water infiltration-induced deterioration and structural failures. Additionally, the work by Xu et al. (2020) provided an infiltration analysis of perforated storm sewers, employing finite difference modeling and field tests to optimize drainage hole design for enhanced stormwater management.

It is important to emphasize several key studies on internal erosion, particularly those employing Computational Fluid Dynamics (CFD) and focusing on erosion around defective pipes. Recent works, such as Zhang et al. (2020), which investigated internal erosion around submerged defective pipes through both experimental and numerical approaches, and Ibrahim and Meguid (2023), which studied sand erosion into defective gravity pipes using CFD-DEM simulations, offer valuable insights into erosion-induced failure mechanisms. These studies demonstrate how water infiltration and the resulting loss of soil particles, known as suffusion, can severely impact the stability of buried pipelines and their overlying structures.

The persistent challenge of addressing leakages in sewer and water pipelines has been a primary concern for water management authorities, giving rise to a myriad of issues from drinking water shortages to groundwater pollution and the consequential emergence of sinkholes. In extreme cases, sinkholes not only jeopardize existing infrastructure but also pose a direct threat to human life, emphasizing the urgent need for robust prevention and monitoring measures. Countries such as Australia, the United Kingdom, France, Spain, and the United States, among others, have grappled with the repercussions of pipeline leaks, experiencing depleted domestic water supplies and complications like subsidence and sinkholes (Kwak et al., 2015).

**Table 1.** Examples of blowout cases induced by water mains bursts.

Date	Location	Cause of catastrophe	Damage	References
10/07/2020	Perth, Australia	The sinkhole formed due water mains burst	No injury, Car swallowed up.	www.abc.net.au, 2020
24/12/2010	Sydney, Australia	Water mains burst near Moore Park, Sydney	Lost many millions of litres of water, and damaged infrastructures.	www.abc.net.au, 2010
19/05/2017	Kyiv, Ukraine	Pipe bursts due to pressure difference	Several nearby cars were damaged and left a 6 m <sup>2</sup> hole in the ground.	Global News, 2017
28/02/2020	Houston, USA	digging to repair a "gradual leak" on the waterline	Water pressure reduction throughout the city, substantial water losses, and infrastructure damage.	Stanglin, 2020
30/08/2016	New York, USA	The pipe burst and caused a sinkhole.	Swallowed up a BMW SUV, road damage.	DNAinfo New York, 2016

Table 1 provides illustrative examples of instances where blowouts resulting from water main bursts have led to catastrophic outcomes, highlighting the diverse causes behind these incidents. Despite the gravity of these occurrences, comprehensive data encompassing soil type, water mains specifications, environmental conditions, and sinkhole geometry often remains elusive, hindering a thorough understanding of the complexities involved (Guo and Zhu, 2017). Additionally, critical criteria influencing the scale of soil erosion due to pipe defects are frequently absent, as media reports tend to provide only a general overview. Urgency in restoring infrastructure swiftly often precludes detailed investigations into the root causes of these incidents (Indiketiya et al., 2019).

In a recent endeavor to address the complexities of sinkhole dynamics, Shiau et al. (2022) delved into the three-dimensional stability of sinkhole "collapse," focusing on various cavity shapes. However, a noticeable research gap persists regarding the "blowout" stability of cover soils subjected to "uplifting" water mains pressure. The current study seeks to bridge this gap by thoroughly investigating soil blowout stability with three distinct idealized cavity shapes—circular, half-sphere, and full-sphere openings. Utilizing advanced 3D Finite element limit analysis (FELA) grounded in upper and lower bound theorems, this research explores blowout stability across an extensive spectrum of depth ratios and shear strength ratios. The outcomes of this investigation extend beyond theoretical inquiry, culminating in the development of design charts and equations that incorporate practical design parameters. These tools empower engineers and practitioners to conduct preliminary assessments of soil blowout stability in real-world scenarios, contributing to both academic knowledge and practical engineering applications.

\*Corresponding author. mail: [nguyentan@tdtu.edu.vn](mailto:nguyentan@tdtu.edu.vn)

Recently, Keawsawasvong and Ukritchon (2019) employed 3D FELA to investigate the undrained stability of spherical cavities in cohesive soils. Their study explores the cover depth ratio and dimensionless overburden factor, revealing discrepancies in a previously recommended lower-bound solution. Through nonlinear regression analysis, they propose a more accurate approximate solution and introduce new cavity stability factors for soil cohesion and unit weight. Emphasizing the three-dimensional effects of cavity shape under axisymmetric and plane strain conditions, their findings offer practical insights for engineering applications. In another recent work, Lai et al. (2023) present a hybrid framework for predicting stability solutions of buried structures under active trapdoor conditions in natural clays. Combining physics-based and data-driven modeling techniques, they use FELA with an anisotropic undrained shear (AUS) failure criterion. Practical considerations for natural clays, including three linearly increasing shear strengths, are integrated into the AUS material model. Validating numerical solutions against published results, they utilize a multivariate adaptive regression splines (MARS) algorithm for fast FELA data-driven surrogates. The MARS-based modeling provides relative importance indices and accurate design equations, offering practitioners reliable tools for stability evaluation. Notably, the application of 3D FELA for Water Main Bursts and Soil Blowout Stability has been absent from the literature, and this study aims to fill this critical gap.

In summary, this study aims to achieve the following objectives: (i) Investigate the stability of water mains under burst conditions using advanced 3D FELA; (ii) Explore the influence of key parameters, including depth ratios and shear strength ratios, on the pressure ratio in the context of soil blowout stability; (iii) Develop design contour charts based on lower and upper bound solutions to provide practical insights for engineers assessing blowout stability; (iv) Compare and validate the 3D FELA results with existing literature, establishing the accuracy and reliability of the proposed approach; (v) Offer a comprehensive understanding of the three-dimensional effects of cavity shape on blowout stability under different conditions, contributing valuable insights for engineering applications. Through these objectives, the study aims to enhance the current understanding of 3D FELA in the context of water main bursts and soil blowout stability, addressing a notable gap in the existing literature.

## 2. Problem Layout and the FELA Modelling

This section presents the examination of blowout stability using three distinct idealized cavity shapes: circular, half-sphere, and full-sphere openings. Fig. 1a-c vividly illustrates the evolution of the pipeline burst problem under high water pressure, depicting the progression from the initial circular stage through the development of half-sphere and full-sphere cavities. Specifically, Fig. 1a portrays the initial blowout stage with no cavity formation, while Fig. 1b and Fig. 1c showcase the subsequent second (half-sphere) and third (full-sphere) stages of cavity development.

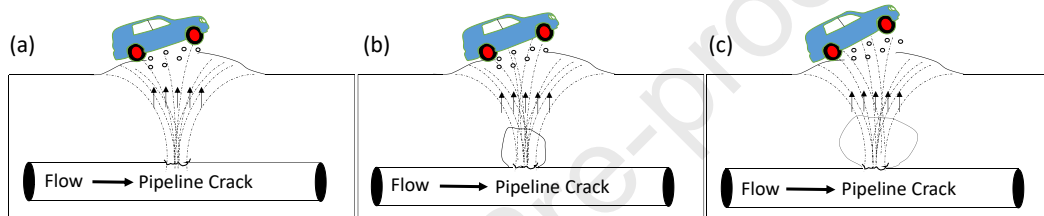


**Fig. 1.** Evolution of internal soil erosion in water main bursts: (a) Initial blowout stage (circular opening), (b) Stage II: Cavity development (half-sphere opening), and (c) Stage III: Cavity development (full-sphere opening).

The configuration depicted in Fig. 1a is conceptualized as an idealized flat circular opening, as demonstrated in Fig. 2, symbolizing the initial stage of a pipeline burst. This flat circular opening, idealised by dimensions of diameter ( $D$ ) and cover depth ( $C$ ), is subjected to analysis with the internal face experiences normal pressure ( $\sigma_i$ ) and the ground surface encounters external surcharge pressure ( $\sigma_s$ ). To accurately represent soil behavior, a simple rigid-plastic material model is utilized, given that bound theorems are exclusively applicable to materials displaying both rigidity and plasticity with associated flow rules. The soil medium is defined using a Tresca soil model, encompassing parameters like undrained shear strength ( $S_u$ ) and unit weight ( $\gamma$ ). It is essential to emphasize that the failure criterion adheres to the Mohr-Coulomb criterion, particularly under conditions featuring a zero-friction angle. The dimensions of the model domain are chosen in such a way that the overall developed velocity field would not intersect with the boundary. This has been confirmed by observing the failure mechanisms, as shown in later contour plots such as Figs. 3, 5, 7, 16, and 17. It is also to be acknowledged that, although a pipe should be buried in well drained materials, it is not uncommon to see the use of in-situ excavated materials during construction.

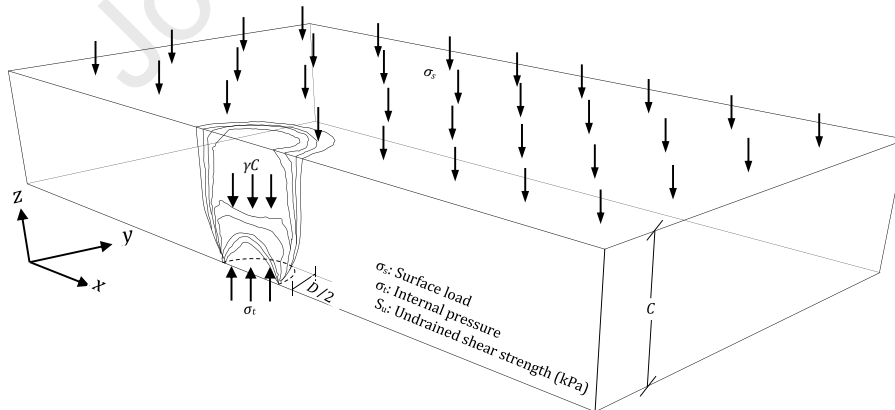


**Fig. 2.** Problem definition (circular opening,  $C/D = 2$ ).

Depicted in Fig. 3 is a representative presentation of the adaptive mesh and the contour plot of absolute velocity ( $|u|$ ) for the conceptualized flat circular opening. To maintain clarity, only half of the 3D mesh is displayed, taking advantage of its symmetrical nature. Additionally, Fig. 3 provides a perspective from the bottom of the flat circular opening.

Regarding boundary conditions, three sides are fixed in the normal direction, while the bottom side is fully constrained in all directions. The top surface is considered a free surface with no imposed restrictions. As for the symmetrical plane, all nodes are restrained in the normal direction, permitting unrestricted tangential movements.

Careful consideration is given to generating the domain in a manner that prevents inadequate boundary conditions from compromising the overall velocity field. This meticulous approach ensures that the study accurately captures the system's behavior, mitigating the risk of introducing artifacts due to limitations in the definition of boundaries.

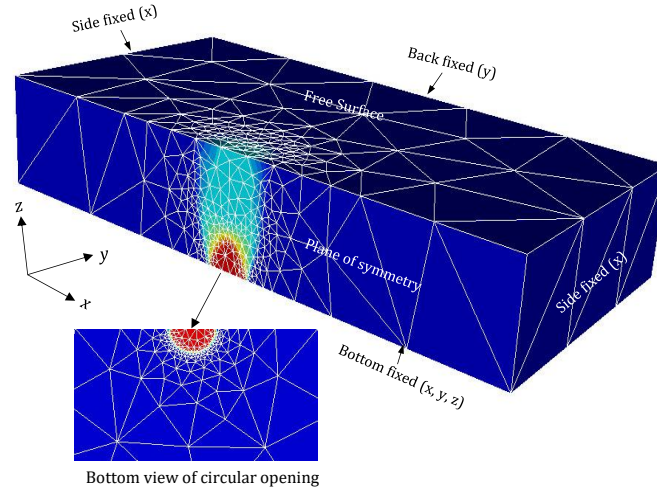


**Fig. 3.** Illustration of a typical adaptive mesh and contour plot of absolute velocity ( $|u|$ ) for the circular opening ( $C/D = 2$ ).

Integrating adaptive mesh refinement into both upper bound (UB) and lower bound (LB) simulations has played a crucial role in accurately determining the limit load. Drawing from the insights provided by Sloan (2013), the derivation of the upper bound solution entails defining a kinematically admissible velocity field, while the lower bound solution involves establishing a statically admissible stress field. By incorporating the bounds gap error estimator within the framework of UB and LB theorems, this approach provides a precise approximation of the bounding solutions. This novel technique has been widely used to evaluate various geotechnical stability problems (Shiau and Smith, 2006; Shiau et al., 2018; Shiau and Al-Asadi, 2021; Payan et al., 2022; Lai et al., 2022; Keawsawasvong et al., 2022; Lai et al., 2023; Nguyen and Shiau, 2023; Shiau et al., 2023). The stability computation, outlined in this study, employs the recently developed 3D FELA—a technique introduced by OptumCE (2020), showcasing a dependable capability to compute 3D limit loads.

The traditional dimensional analysis of the six design parameters ( $\sigma_s, \sigma_c, C, D, \gamma, S_u$ ) yields four dimensionless groups, namely:  $\sigma_s/S_u, \sigma_c/S_u, C/D$ , and  $\gamma D/S_u$ .

Recognizing that geophysical techniques can provide insights into cavity location and size, thereby influencing the values of  $C$  and  $D$ , a thorough site investigation becomes imperative for obtaining accurate soil property values ( $\gamma$  and  $S_u$ ). The conventional approach involves consolidating the first two groups into a unified entity, denoted as  $(\sigma_s - \sigma_c)/S_u$ , especially under the undrained condition of the problem (Shiau and Hassan, 2021; Shiau et al., 2022). Typically, refining the existing FELA method often requires specifying either the parameter ( $\sigma_s$  or  $\sigma_c$ ). This study introduces the joint term  $(\sigma_s - \sigma_c)/S_u$  as the pressure ratio ( $PR$ ), which depends on both the depth ratio ( $C/D$ ) and the strength ratio ( $\gamma D/S_u$ ). As described in Eq. (1), this combination carefully evaluates the pressure disparity between the surface surcharge ( $\sigma_s$ ) and the cavity pressure ( $\sigma_c$ ):

$$PR = \frac{\sigma_s - \sigma_c}{S_u} = f\left(\frac{C}{D}, \frac{\gamma D}{S_u}\right) \quad (1)$$

A comprehensive investigation was conducted, spanning various depth ratios ( $C/D = 0.5 - 4$ ) and shear strength ratios ( $\gamma D/S_u = 0 - 2$ ) to assess the soil blowout stability of the flat circular opening. The study scrutinized a total of seventy blowout failures using both lower and upper bound limits of the pressure ratio ( $PR$ ). The optimization process focused on improving the critical blowout pressure ( $\sigma_c$ ) as the objective function. The parameters subject to design, collectively termed the "designed" parameters, encompass  $C, D, \sigma_s, \gamma$ , and  $S_u$  and serve as the program inputs. Determination of  $PR$  values involved substituting the critical supporting pressure ( $\sigma_c$ ) into the  $PR$  equation, contingent on the dimensionless ratios ( $C/D$  and  $\gamma D/S_u$ ).

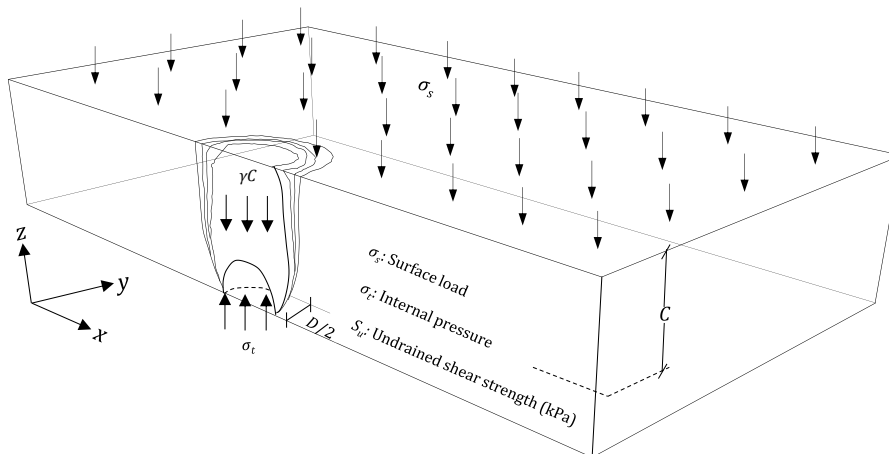


**Fig. 4.** Problem definition for a half-sphere opening with  $C/D$  of 2.

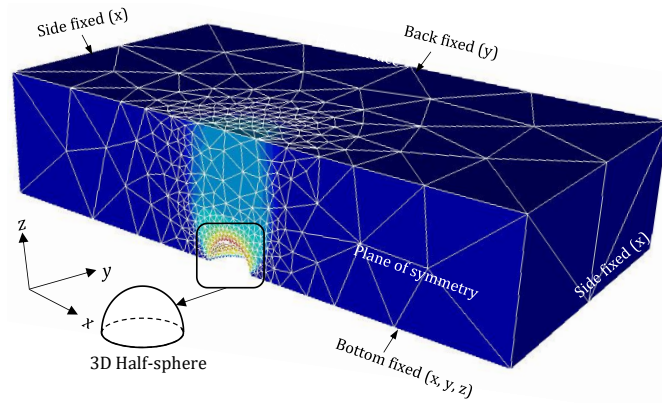


**Fig. 5.** Typical adaptive mesh alongside the contour plot of absolute velocity ( $|u|$ ) for a half-sphere opening with  $C/D$  of 2.

The problem statement remains consistent for both the second stage, involving the half-sphere cavity illustrated in Fig. 4 and Fig. 5, and the third stage, presenting the full-sphere cavity in Fig. 6 and Fig. 7. It's crucial to emphasize that  $C$  denotes the soil cover extending from the ground surface to the crown of the cavity. It is noted that, for pipe engineers, the term of burial depth is more often used. The optimization focus is on the internal cavity surface pressure ( $\sigma$ ), specifically in the normal direction. A summary of the study plan with selected parameters is shown in Table 2.

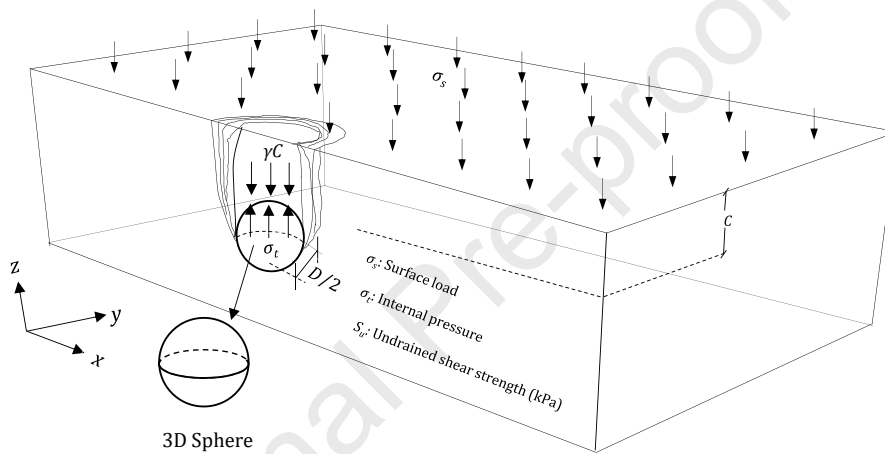


**Fig. 6.** Definition of a full-sphere opening with  $C/D$  of 2.

**Table 2.** Summary of the studied parameters.

Stages	Depth ratio ( $C/D$ )	Strength ratio ( $\gamma D/S_u$ )
Stage 1 (Fig. 2 – flat circular opening)	0.5, 1.0, 1.5, 2.0, 2.5, 3.0, 3.5, and 4.0	0.5, 1.0, 1.5, and 2.0
Stage 2 (Fig. 4 – half-sphere opening)	0.5, 1.0, 1.5, 2.0, 2.5, 3.0, 3.5, and 4.0	0.5, 1.0, 1.5, and 2.0
Stage 1 (Fig. 6 – full-sphere opening)	0.5, 1.0, 1.5, 2.0, 2.5, 3.0, 3.5, and 4.0	0.5, 1.0, 1.5, and 2.0

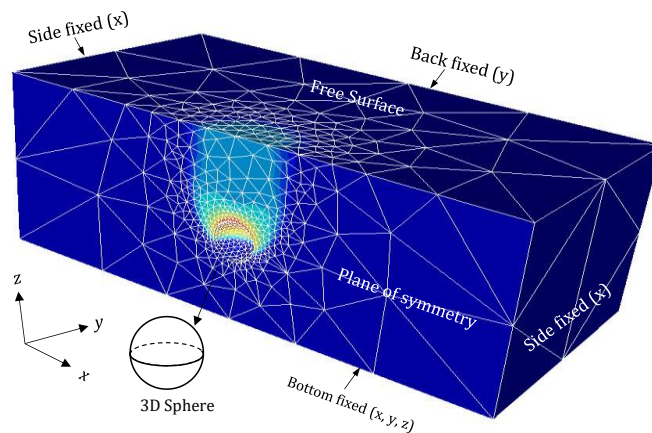


**Fig. 7.** Illustration of adaptive mesh and velocity contours for a full-sphere opening ( $C/D = 2$ ).

### 3. Results and Discussion

#### 3.1. Blowout Stability

In this section, the analysis rigorously scrutinizes the blowout stability resulting from water main bursts, leveraging the sophisticated 3D FELA technique, which integrates both upper and lower theorems. The main emphasis is to demonstrate blowout stability by examining the  $PR$  across three different cavity shapes: the flat circular, the half-sphere, and the full-sphere. Numeric outcomes are concisely displayed in Fig. 8 through Fig. 13, covering a range of dimensionless depth ratios, i.e.  $C/D = 0.5$  to 4.0.

Figs 8-13 intricately illustrate the  $PR$  plotted against the depth ratio ( $C/D$ ) for different values of the strength ratio ( $\gamma D/S_u$ ). The selected  $\gamma D/S_u$  range, spanning from 0 to 2.0, deliberately covers the practical parametric range observed in real-world scenarios. This in-depth exploration not only sheds light on the dynamics of blowout stability across varied cavity shapes but also fosters a nuanced understanding of the intricate interplay between pressure ratios, depth ratios, and strength ratios. The parameterized investigation ensures that the insights gained are not only thorough but also directly applicable across a diverse range of real-world scenarios related to water main bursts.

As illustrated in Fig. 2, the occurrence of blowout hinges on the compressive normal "blowout" pressure ( $\sigma_i$ ) surpassing the compressive surcharge pressure ( $\sigma_s$ ). Consequently, negative values of  $PR$  are inherently present in this ongoing blowout study. Exploring the initial stage scenario involving a flat circular opening (see Fig. 1a, Fig. 2, and Fig. 3), Fig. 8 reveals the complex connections between the  $PR$  and the  $C/D$  across different shear strength ratios, i.e.  $\gamma D/S_u = 0-2$ . Notably, the  $PR$  demonstrates a nonlinear decline as the  $C/D$  increases for each value of  $\gamma D/S_u$ .

As indicated by the definition of  $PR$ , a decrease in negative coordinates implies a rise in compressive normal "blowout" pressure ( $\sigma_i$ ). The magnitude of  $\gamma D/S_u$  value directly indicates the system's strength or massiveness, requiring a higher value of  $\sigma_i$  to initiate blowout failure. A noteworthy observation is the consistent superiority of UB value of  $\sigma_i$  over LB value of  $\sigma_i$  in the negative coordinate, indicating that an exact solution consistently falls within the confines of both the UB and LB. This alignment provides a reliable bracketing of the solution.

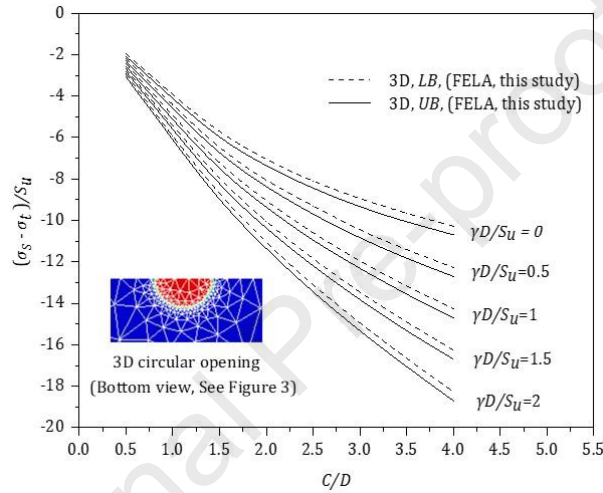


**Fig. 8.** Stability results for stage I (circular opening).

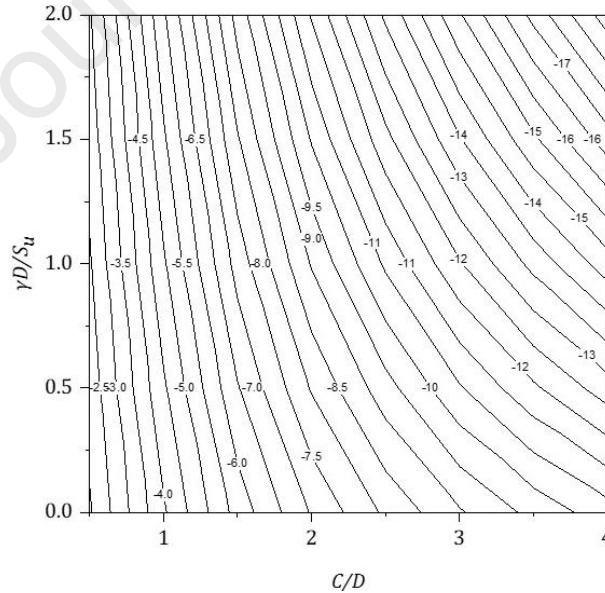


**Fig. 9.** Design chart corresponding to stage I, focusing on the circular opening.

Fig. 9 illustrates a design contour chart specifically tailored for the flat circular opening issue. Within this blowout stability chart, the  $x$ -axis delineates the depth ratio ( $C/D$ ), whereas the  $y$ -axis represents the strength ratio ( $\gamma D/S_u$ ). Negative contour values on the chart signify the  $PR$ , a metric to be derived by design engineers based on their designated parameters like  $C/D$  and  $\gamma D/S_u$ . These design charts serve as practical tools for conveniently assessing critical blowout pressures ( $\sigma_i$ ) across the three distinct cavity shapes.

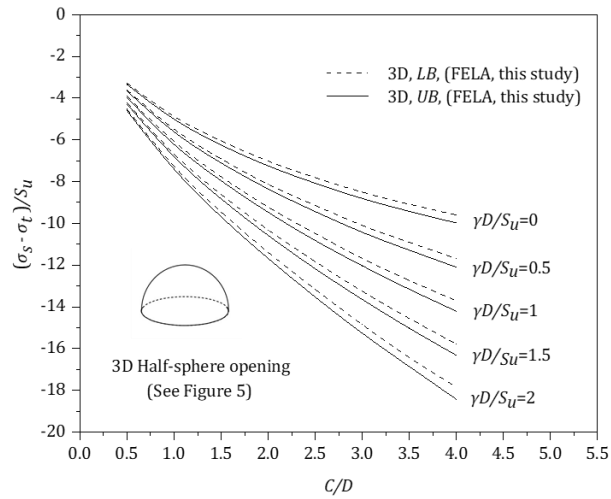


**Fig. 10.** Stability results for stage II, featuring the half-sphere opening.

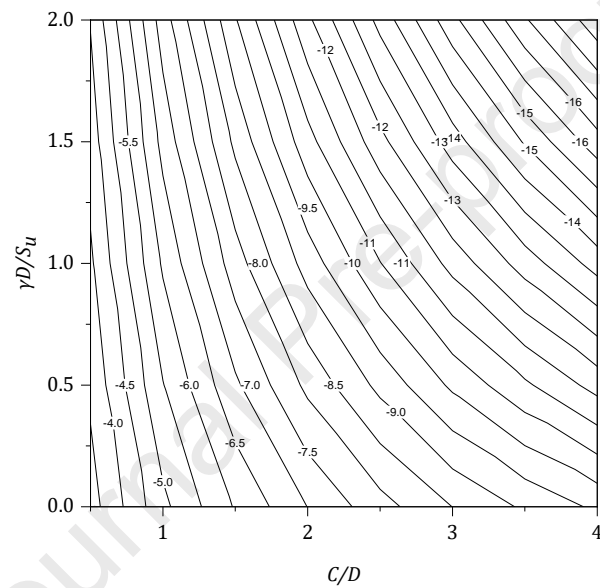


**Fig. 11.** Design chart for stage II, focusing on the half-sphere opening.

When juxtaposed with the stage one scenario involving a flat circular opening, analogous patterns emerge in the stage two issues (Figs. 10–11; half-sphere opening) and the stage three problems (Figs. 12–13; full-sphere opening). Consequently, a significant examination of  $PR$  across the three distinct shapes is delineated in the subsequent section.

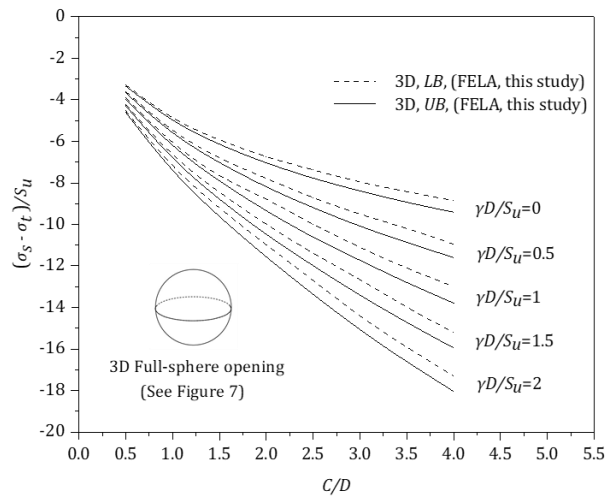


**Fig. 12.** Stability results for Stage III, specifically for the full-sphere opening.

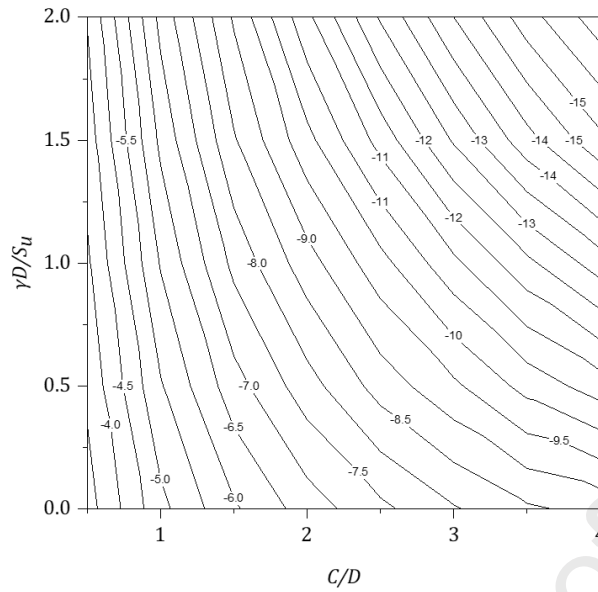


Fig.13. Design chart for stage II, focusing on the full-sphere opening.

### 3.2. Comparative analysis of three cavity shapes

In the investigation of internal soil erosion processes manifested through three idealized cavity shapes, a pivotal aspect entails an in-depth comparison of their respective influences on blowout stability. This comprehensive scrutiny unfolds in Fig. 14, wherein the  $PR$  is graphically portrayed against the  $C/D$  for each of the three distinctive cavity shapes. Notably, the selected strength ratios i.e.,  $\gamma D/S_u = 0$  and 1, enable a nuanced examination of how varying soil strength conditions influence blowout stability across different cavity configurations.

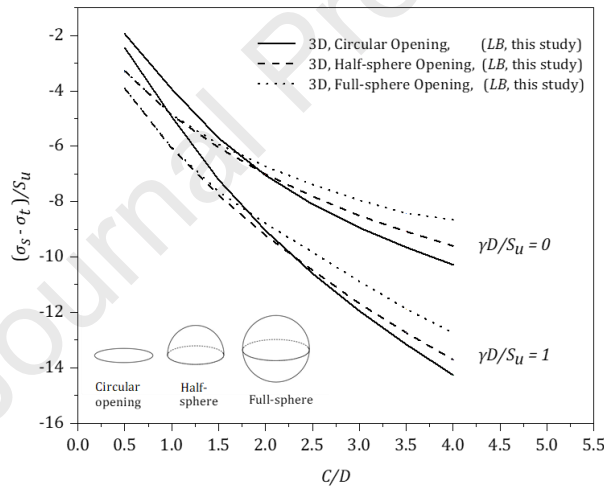
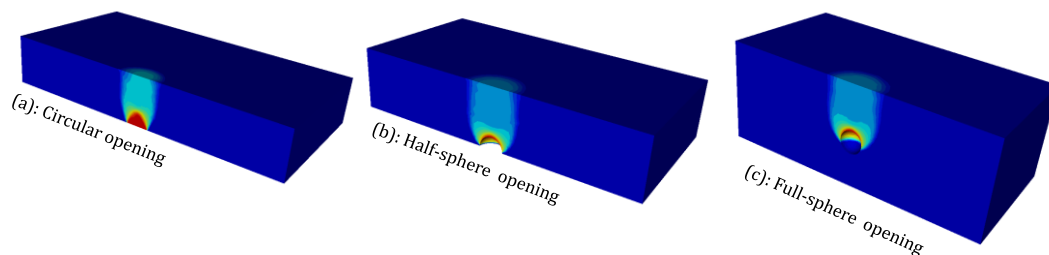


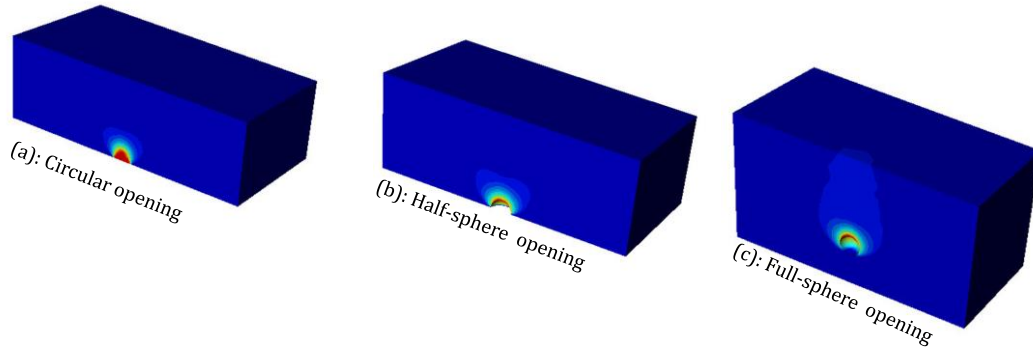
Fig. 14. A comparative analysis of three different cavity shapes.

Fig. 14 elucidates that, within the realm of shallow depths ( $C/D < 1.75$  and  $\gamma D/S_u = 0$ ), comparable  $PR$  values manifest for both half- and full-sphere openings. This parallelism extends to scenarios where  $\gamma D/S_u = 1$  holds true, particularly when  $C/D < 2.0$ . The augmented stability exhibited by half- and full-spheres in these shallow instances, attributed to their curved configurations facilitating isotropic stress distribution, is underscored by their higher absolute  $PR$  values in contrast to the flat circular opening.

Notably, a discernible shift in trend emerges with increasing of  $C/D$ . The absolute  $PR$  for the flat circular opening surpasses that of the other two shapes. This underscores the imperative consideration of all shapes - circular, half-sphere, and full-sphere in the assessment process, as the outcomes exhibit dynamic variations in response to alterations in the depth ratio.



**Fig. 15.** A comparative assessment of blowout failures across the three cavity shapes at a depth ratio ( $C/D$ ) of 2 and a shear strength ratio ( $SR$ ) of 1: (a) Circular opening, (b) Half-sphere opening, and (c) Full-sphere opening.



**Fig. 16.** A comparative analysis of blowout failures across three different cavity shapes, conducted at a depth ratio ( $C/D$ ) of 4 and a shear strength ratio ( $SR$ ) of 1: (a) Circular opening, (b) Half-sphere opening, and (c) Full-sphere opening.

Fig. 15 and Fig. 16 present an in-depth visual exploration using absolute velocity ( $|u|$ ) contour plots for circular, half-sphere, and full-sphere openings. This comparative investigation examines different depths ( $C/D = 2$  and  $4$ ,  $\gamma D/S_u = 1$ ) for each cavity shape. It's crucial to note that, given the perfectly plastic soil model (Shiau and Al-Asadi 2020b), the specific values of the colored contours hold limited importance. The focus shifts towards identifying shear bands and comprehending the nuanced failure mechanisms.

At shallower depths (see Fig. 15 with  $C/D = 2$ ), a uniform presence of global blowout failure mechanisms is evident across all three shapes. However, with an increase in the depth ratio (see Fig. 16 with  $C/D = 4$ ), a noticeable transition to localized blowout failure mechanisms is observed for each unique opening shape. This detailed analysis provides deeper insights into the dynamic behavior of these cavity shapes under varying conditions, enhancing our understanding of blowout stability assessment. It should be noted that there is no criterion for identifying the cases of shallow burial depth and deep burial depth criterion. The terms are used to describe a deep local failure mechanism and a shallow global failure extending to the ground surface.

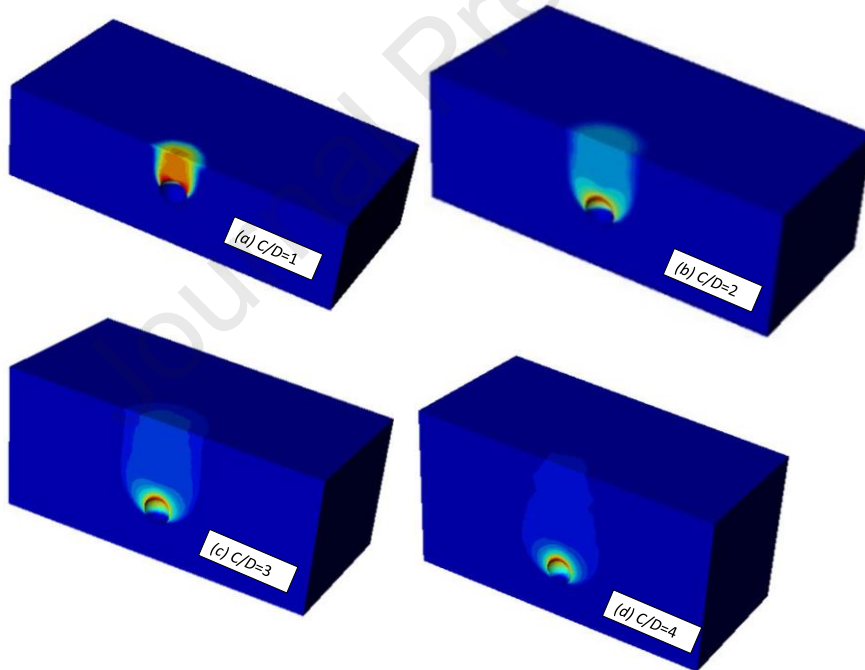


**Fig. 17.** Contour plots depicting the absolute velocity ( $|u|$ ) distribution for the full-sphere opening during blowout failures ( $C/D = 1-4$ ,  $\gamma D/S_u = 1$ ): (a)  $C/D=1$ , (b)  $C/D=2$ , (c)  $C/D=3$ , and (d)  $C/D=4$ .

In the discipline of geotechnical stability modelling using FELA, the contour plots are for representing non-zero velocity field. In this way, the potential failure mechanism can be examined. Noting that the absolute values of the velocity fields are not important, therefore we do not show the legend. It is just for illustrating the possible failure mechanism of blowout scenarios, as mainly for this study. In Fig. 17, a supplementary contour plot is presented to illuminate the intricate blowout failure mechanisms within a full-sphere cavity. Covering a spectrum of depth ratios ( $C/D = 1$  to  $4$ ) while maintaining a consistent strength ratio i.e.,  $\gamma D/S_u = 1$ , this visual representation provides essential insights into the diverse blowout failure shapes manifested on the ground surface. The plots depict nearly perfect circles, reminiscent of the characteristic formations observed in sinkholes worldwide. Notably, as the  $C/D$  ratio ascends, a discernible shift in failure mechanisms is observed - from a global nature in shallow cases to a more localized pattern in deeper scenarios. This detailed exploration significantly contributes to our comprehensive understanding of blowout stability mechanisms under varying conditions.

### 3.3. Comparison with published results

Given the paucity of published results on blowout stability, this study endeavors to validate and compare its numerical solutions. The comprehensive assessment involves contrasting outcomes with the results from three-dimensional trapdoor studies (Shiau et al., 2021), three-dimensional circular tunnel heading investigations (Shiau and Al-Asadi, 2020a), and other pertinent findings. Fig. 18 specifically delves into the circular opening

(trapdoor), with detailed data meticulously outlined in Table 3. Past studies commonly utilized Broms and Bennermarks' stability number, employing a critical stability number ( $N_c$ ) that incorporates surcharge ( $\sigma_s$ ), soil self-weight ( $\gamma H$ ), and supporting pressure ( $\sigma_t$ ). To facilitate a meaningful comparison, the  $N_c$  is converted to the  $PR$ , assuming zero-unit weight of soil ( $\gamma$ ). This conversion aligns the  $N_c$  with our  $PR$  values.

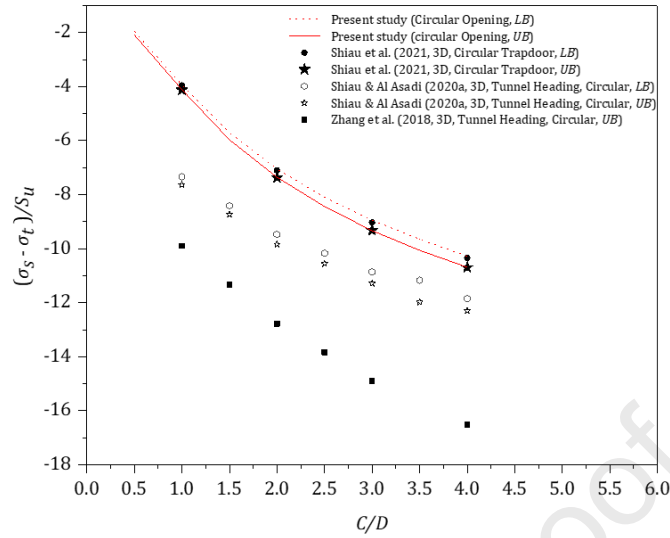


Fig. 18. Comparative analysis with published findings.

Table 3. A comparison with previously published findings.

$C/D$	Zhang et al. (2018) (UB)	Shiao and Al-Asadi (2020a) (UB)	Shiao and Al-Asadi (2020a) (LB)	Shiao et al. (2021) (UB)	Shiao et al. (2021) (LB)	Present study (UB)	Present study (LB)
0.5						-2.08	-1.95
1	-9.9	-7.64	-7.34	-4.12	-3.96	-4.11	-3.93
1.5	-11.34	-8.74	-8.41			-5.97	-5.70
2	-12.78	-9.84	-9.47	-7.37	-7.1	-7.36	-7.05
2.5	-13.84	-10.56	-10.17			-8.44	-8.10
3	-14.9	-11.29	-10.86	-9.32	-9.03	-9.33	-8.94
3.5		-11.98	-11.17			-10.06	-9.65
4	-16.53	-12.31	-11.85	-10.7	-10.34	-10.69	-10.28

Our current research findings align significantly with the results reported by Shiao et al. (2021) for the 3D circular trapdoor scenario, indicating a strong agreement. However, a noteworthy observation arises when contrasting these outcomes with those of the 3D circular tunnel heading, specifically the vertical circular trapdoor, as detailed in Shiao and Al-Asadi (2020a). In this comparison, their results consistently show higher absolute  $PR$  values than our study, highlighting a notable discrepancy. This divergence persists despite the inherent differences in the problem formulations, considering both horizontal and vertical trapdoors.

For instance, in the study by Shiao and Al-Asadi (2020a), it was found that at  $C/D = 1$ , the lower bound value of  $PR$  for investigating the horizontal circular trapdoor is 4.97, while that for the 3D tunnel heading was 7.34. The difference between these values, calculated as  $[(7.34 - 4.97)/7.34 \times 100 = 32.29\%]$  gradually decreases to  $[(12.31 - 9.41)/12.31 \times 100 = 23.5\%]$  at  $C/D = 4$ . This reduction in the percentage gap between the two trapdoors (horizontal and vertical) is attributed to a transition in failure mechanisms from global (in shallow cases) to local (in deep cases) as the  $C/D$  ratio increases.

Zhang et al. (2018) utilized an analytical upper-bound approach to ascertain the failure pressure of a 3D tunnel heading. This method relies on predefined assumptions regarding the general form of the failure surface, resulting in solutions of lower precision, as noted by Sloan (2013). The analytical upper bounds tend to be notably conservative, as visually illustrated in the accompanying Fig. 18.

In light of the distinct nature of horizontal and vertical trapdoor scenarios, the inclusion of this comparison is deemed necessary due to the limited literature on 3D passive trapdoor studies. This intriguing observation, highlighting the vertical circular trapdoor's superior resistance to blowout failure when contrasted with its horizontal counterpart, adds a compelling dimension to the paper.

### 3.4. Comparison with an axisymmetric model

To enhance the robustness of our 3D findings, we've introduced an axisymmetric model (AX) for a comprehensive comparative analysis. This approach condenses the intricacies of 3D scenarios into more manageable 2D representations, significantly reducing computational time. Fig. 19 illustrates a representative axisymmetric adaptive mesh, comprising a total of 10,000 elements. Nodes along the axis of symmetry are restricted from moving in the normal direction but retain the freedom for vertical shifts. While numerous notations and boundary conditions were previously elucidated and won't be reiterated, this AX serves as a pivotal benchmark for result validation and efficiency assessment.

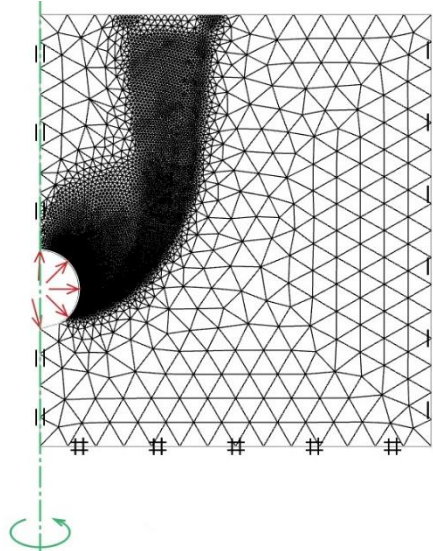


Fig. 19. Typical mesh in axisymmetric analysis.

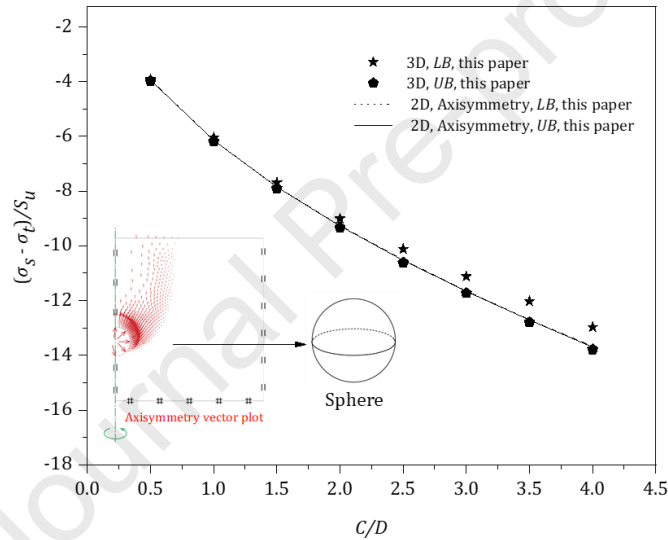


Fig. 20. Comparative analysis of 3D and 2D axisymmetric models.

The application of an extensive number of elements in the AX within this study has resulted in highly precise numerical outcomes. As illustrated in Fig. 20, where the 2D AX UB and AX LB align closely on the same curve, it is evident that the 3D LB solutions could be further refined with an increased number of 3D elements. In summary, this comparison underscores a substantial concordance between the 3D and 2D axisymmetric models, significantly bolstering confidence in the accuracy and reliability of the current 3D results.

#### 4. Practical examples

The design contour charts presented in Fig. 9, Fig. 11, and Fig. 13 are based on the lower bound solutions, providing a robust assessment of the critical blowout pressure ( $\sigma_t$ ). Let's delve into an illustrative example that elucidates the process of determining factors of safety ( $FoS$ ) for a three-staged problem, as depicted in Fig. 21. The scenario involves the blowout stability assessment of a flawed pipeline.

##### 4.1. Water main burst scenario:

In the water main burst scenario, the internal pressure of the water mains is assumed to be 175 kPa during the pipeline failure. The ground is subjected to a surcharge pressure ( $\sigma_s$ ) of 2 kPa. The pipeline is considered to have a crack width ( $D$ ) of 0.25 meters. The undrained shear strength ( $S_u$ ) of the surrounding soil is taken as 26 kPa, and the unit weight of the soil ( $\gamma$ ) is 16 kN/m<sup>3</sup>.

##### 4.2. Three Stages of Sinkhole Formation (Fig. 21)

In the initial stage, represented by a flat circular opening (see Fig. 21a), the cover depth is 0.75 m and the opening width is 0.25 m, resulting in a depth ratio ( $C/D$ ) of 3. The strength ratio is calculated as  $\gamma D / S_u = (16 \times 0.25) / 26 = 0.153$ . According to Fig. 9, the corresponding critical pressure ratio ( $PR$ ) is  $-9.0$ . The critical blowout pressure ( $\sigma_t$ ) is therefore determined to be 236 kPa. Since the applied water main pressure of 175 kPa is less than this critical value, the factor of safety ( $FoS$ ) is  $236 / 175 = 1.34$ , indicating a stable condition.

In the intermediate stage, modeled as a half-sphere opening (see Fig. 21b), the cover depth is reduced to 0.65 m, while the opening width remains at 0.25 m, giving a  $C/D$  of 2.6. The strength ratio remains unchanged at 0.153. From Fig. 11, the critical  $PR$  is  $-8.1$ , and the corresponding critical blowout pressure is calculated as 212.6 kPa. With the applied water main pressure still at 175 kPa, the factor of safety is reduced to  $212.6 / 175 = 1.21$ , indicating a lower but still safe condition.

In the final stage, characterized by a full-sphere opening (see Fig. 21c), the cover depth further decreases to 0.4 m, while the opening width remains at 0.25 m, resulting in a  $C/D$  of 1.6. The strength ratio remains at 0.153. Based on Fig. 13, the critical  $PR$  is  $-6.2$ , leading to a critical blowout pressure

of 163.2 kPa. In this case, the applied water main pressure of 175 kPa exceeds the critical pressure, and thus blowout failure is expected to occur. The factor of safety drops below unity, with a value of  $163.2/175 = 0.93$ .

In essence, the prevention of blowout failure hinges on maintaining the applied water mains pressure below the calculated theoretical blowout pressure ( $\sigma_t$ ). This crucial relationship emphasizes the significance of  $FoS$ , which naturally decline as the cavity size increases - a trend that mirrors real-world scenarios. Notably, a transformation in the scenario is presented from an impending blowout to a collapse problem, marked by the presence of an existing internal cavity. This understanding emphasizes the dynamic interplay of pressure management and structural stability in the context of pipeline design and integrity.

Please note that, in this example, we aim to demonstrate on the use of dimensionless design charts. As discussed before, when it is dimensionless, a series of parametric designs becomes flexible. Noting that the ideal pressure at outlets should be at least 150kPa, we therefore chose 175 kPa in this example. The overburden soil pressure has been included in the internal computation with soil unit weight given in the FELA model. Therefore, the ground surface pressure is only given as 2 kPa, representing additional surface pressures coming from traffics or machineries. The undrained shear strength is 26 kPa, that would be used to demonstrate this blowout example.

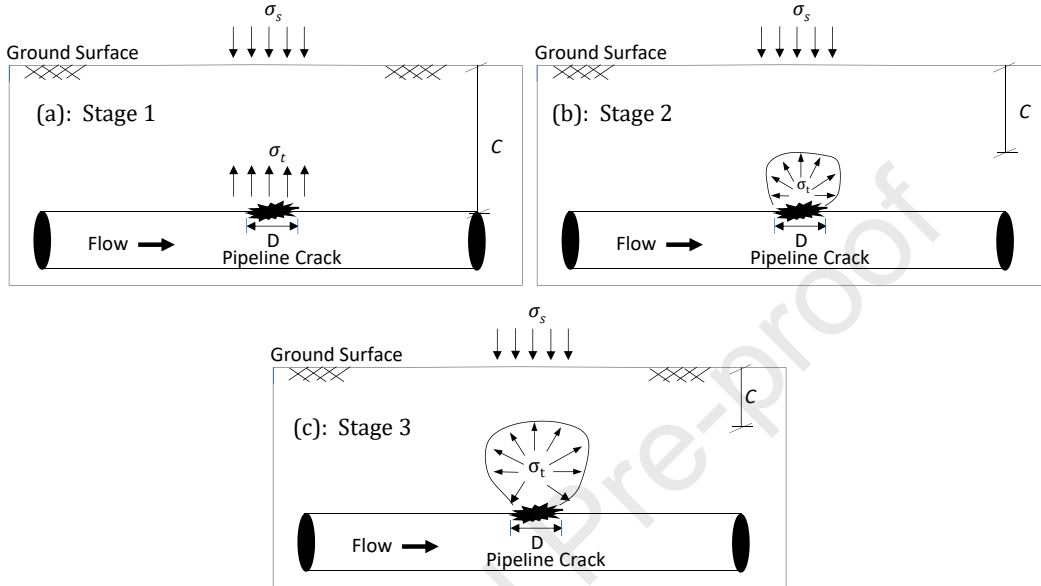


Fig. 21. Three stages of Sinkhole Formation: (a) Stage 1, (b) Stage 2, and (c) Stage 3.

## 5. Conclusions

This paper has made a significant contribution in investigating soil blowout stability resulting from water mains bursts. It utilized advanced 3D FELA in conjunction with classical lower and upper bound theorems, as well as an adaptive finite element mesh technique. The study explored the impact of depth ratio and shear strength ratio on the pressure ratio across three idealized cavity shapes. Relationships among cover depth ratio ( $C/D$ ), shear strength ratio ( $\gamma D/S_u$ ), and pressure ratio ( $PR$ ) were established through the development of design contour charts, offering valuable insights into the complex interactions of these critical parameters. Notably, the findings revealed the extent of circular surface failure and the transformation of failure mechanisms with increasing depth ratio. To enhance the reliability of the results, an axisymmetric model was introduced for comparison with a full 3D analysis. Illustrative examples were provided to demonstrate the procedure for evaluating blowout stability.

## 6. Limitation and future work

Recent tests on HDD have helped us better understand borehole stability and how mud flows. However, this study focuses on a different problem: blowout failure in shallow pipelines under roads. This issue is not the same as those studied in HDD. Lan and Moore (2022) looked at how pump rates affect borehole stability and found important details about mud speeds and ground movements. In another study, Lan and Moore (2020) examined how the depth of the borehole impacts stability, identifying the highest mud pressure and paths of mudflow. Lan et al. (2024) also studied how mud moves and spreads, explaining why boreholes become unstable. While these HDD studies provide useful information, they involve conditions that are very different from those of shallow pipelines. Shallow pipelines are more likely to fail locally and cause sinkholes, especially if the pipelines are damaged.

Specifically, shallowly buried pipelines are typically found at shallow depths beneath roadways, where pressurized water escaping from damaged pipelines can cause localized ground failure and even sinkholes. In contrast, HDD involves deeper boreholes that are stabilized by injecting mud, which changes how fluids behave and how failures occur. While some comparisons can be made, such as comparing mud pressure in HDD to water pressure in this study, there are major differences. These include boundary conditions, fluid properties, and depth factors, which make separate modeling approaches necessary. As a result, adapting HDD simulations to the current blowout failure model would require significant changes that go beyond the scope of this study.

Despite these differences, some similarities, such as fluid-induced failure mechanisms, are acknowledged. For example, mud pressure in HDD can be compared to water pressure in this study, and a defective pipeline can be considered similar to a borehole. However, applying HDD-related simulations to the current model would require significant adjustments, including modifications to boundary conditions, fluid properties, and depth parameters. These changes go beyond the scope of this study, which focuses specifically on shallow sinkhole formations caused by pipeline defects.

In practice, sinkhole formation is often associated with soil erosion and influenced by factors such as pavement and foundation structures, which can alter the resisting forces against blowout failure. This study assumes uniform pressure across the cavity and does not account for the effects of erosion on cavity shape, which may result in either conservative or non-conservative predictions. These simplifications highlight the need for further verification and refinement of the model. Moreover, the Tresca model was used as the soil constitutive model in this study due to its simplicity under undrained conditions. While suitable for a preliminary investigation, it is acknowledged that more advanced constitutive models may be necessary to fully capture the complex behavior of soil during blowout conditions.

Although the findings of this study were compared and validated against other analytical solutions, future research should prioritize experimental investigations of blowout failures. Such experiments would provide empirical data to further validate and refine the model. Another key direction for future work is the incorporation of soil random fields and probabilistic approaches to account for variability in soil properties and their impact on blowout stability. This would lead to a more thorough understanding of the factors contributing to blowout failure and support the development of more robust and reliable predictive models.

#### Declaration of competing interest

The authors declare that they have no known competing financial interests or personal relationships that could have appeared to influence the work reported in this paper.

#### Acknowledgements

The authors would like to sincerely thank the anonymous reviewers for their valuable comments and constructive suggestions, which have greatly improved the quality of this manuscript.

#### References

- Cao, Y., Xu, M., Ni, P., and Mei, G., 2022. Physical and numerical modelling of infiltration from drainage holes for perforated storm sewer. *Acta Geotech.* 17(2), 527-543.
- De Waele, J, Gutiérrez, F, Parise, M & Plan, L 2011. Geomorphology and natural hazards in karst areas: A review. *Geomorphology*, 134 (1-2),1–8. DNAinfo New York. (n.d.). Sinkhole Swallows SUV After Water Main Break on the Upper West Side. <https://www.dnainfo.com/new-york/20160830/upper-west-side/sinkhole-from-water-main-break-swallows-suv-on-upper-west-side/>. (Accessed 31 Dec. 2020).
- Global News. (n.d.). Water pipe explodes in Ukraine sending pavement flying, water gushing. <https://globalnews.ca/news/3490956/kyiv-waterpipe-explosion/>. (Accessed 31 Dec. 2020).
- Guo, S. & Zhu, D.Z., 2017. Soil and Groundwater Erosion Rates into a Sewer Pipe Crack. *J. Hydraul. Eng.*, 143(7), 06017008.
- Ibrahim, A., & Meguid, M. A., 2023. CFD-DEM simulation of sand erosion into defective gravity pipes under constant groundwater table. *Tunn. Undergr. Space Technol.*, 131, 104823.
- Indiketiya, S., Jegatheesan, P., Rajeev, P. & Kuwano, R., 2019. The influence of pipe embedment material on sinkhole formation due to erosion around defective sewers. *Transp. Geotech.*, 19, 110–125.
- Keawsawasvong, S. and Ukritchon, B., 2019. Undrained stability of a spherical cavity in cohesive soils using finite element limit analysis. *J. Rock Mech. Geotech. Eng.*, 11(6), 1274-1285.
- Keawsawasvong, S., Shiau, J., Yoonirundorn, K., 2022. Bearing capacity of cylindrical caissons in cohesive-frictional soils using axisymmetric finite element limit analysis. *Geotech. Geol. Eng.*, 40 (7), 3929-3941.
- Kwak, P.J., Park, S.H., Choi, C.H, Lee, H.D., Kang, J.M. & Lee, I.H., 2015, 'IoT(Internet of Things)-based Underground Risk Assessment System Surrounding Water Pipes in Korea', *Int. J. Autom. Control.*, 8( 11), 183–190.
- Lan, H., and Moore, I.D., 2022. New design equation for maximum allowable mud pressure in sand during horizontal Directional drilling. *Tunn. Undergr. Space Technol.*, 126, 104543.
- Lai, F., Chen, F., Liu, S., Keawsawasvong, S, Shiau, J., 2022. Undrained stability of pit-in-pit braced excavations under hydraulic uplift. *Undergr. Space*, 7 (6), 1139-1155.
- Lai, F., Shiau, J., Keawsawasvong, S., Chen, F., Banyong, R. and Seehavong, S., 2023. Physics-based and data-driven modeling for stability evaluation of buried structures in natural clays. *J. Rock Mech. Geotech. Eng.*, 15(5), 1248-1262.
- Lai, V.Q., Shiau, J., Promwichai, T., Limkatanyu, S., Banyong, R., and Keawsawasvong, S., 2023. Modelling soil stability in wide tunnels using FELA and multivariate adaptive regression splines analysis. *Model. Earth Syst. Environ.* 9, 2993–3008.
- Lan, H. and Moore, I.D., 2020. Experimental investigation examining influence of burial depth on stability of horizontal boreholes in sand. *J. Geotech. Geoenviron.*, 146(5), 04020013.
- Lan, H. and Moore, I.D., 2022. Experimental investigation examining influence of pump rates on horizontal borehole stability in sand. *Tunn. Undergr. Space Technol.*, 127, 104608.
- Lan, H., Yan, X. and Moore, I.D., 2024. Mud infiltration and travel paths during mud loss experiments on horizontal borehole stability. *Tunn. Undergr. Space Technol.*, 144, 105565.
- Liu, K., Qiu, R., Su, Q., Ni, P., Liu, B., Gao, J., and Wang, T., 2021. Suffusion response of well graded gravels in roadbed of non-ballasted high speed railway. *Constr. Build. Mater.*, 284, 122848.
- Nguyen, T. and Shiau, J., 2023. Revisiting active and Passive Earth pressure problems using Three Stability factors. *Comput. Geotech*, 163, p.105759. OptumCE 2020, OptumG3. Copenhagen, Denmark: Optum Computational Engineering. See <https://optumce.com/>.
- Payan M., Fathipour H., Hosseini, M., Chenari, R.J., Shiau J., 2022. Lower bound finite element limit analysis of geo-structures with non-associated flow rule. *Comput. Geotech.* 147, 104803
- Qin, X., and Moore, I.D., 2022. Laboratory investigation of backfill erosion around rigid pipes with defective joints. *Géotechnique*, 72(10), 847-859.
- Shiau, J, Smith, C. 2006, Numerical analysis of passive earth pressures with interfaces. Proceedings of the III European Conference on Computational Mechanics (ECCM 2006), 5-8 June 2006, Lisbon, Portugal.
- Shiau J., Sams M., Al-Asadi F., Hassan, M.M., 2018. Stability charts for unsupported plane strain tunnel headings in homogeneous undrained clay. *INT. J. GEOMATE.*, 14 (41), 19-26.
- Shiau, J. & Al-Asadi, F., 2020a. Three-Dimensional Analysis of Circular Tunnel Headings Using Broms and Bennermark's Original Stability Number. *Int. J. Geomech.*, 20(7), 06020015.
- Shiau, J. & Al-Asadi, F., 2020b. Stability analysis of twin circular tunnels using shear strength reduction method. *Geotech. Lett.*, 10(2), 311-319.
- Shiau, J., Lee, J.S. & Al-Asadi, F., 2021. Three-dimensional stability analysis of active and passive trapdoors. *Tunn. Undergr. Space Technol.*, 107, 103635.
- Shiau, J., Keawsawasvong, S., Lee, J.S. and Hassan, M.M., 2022. Three-dimensional circular trapdoor stability. *Transp. Infrastruct. Geotechnol.*, 9(2), 173-184.
- Shiau, J. & Al-Asadi, F., 2021. Twin Tunnels Stability Factors  $F_c$ ,  $F_s$  and  $F_y$ . *Geotech. Geol. Eng.*, 39, 335-345.
- Shiau, J., Chudal, B. & Keawsawasvong, S., 2022 Three-dimensional sinkhole stability of spherical cavity. *Acta Geotech.* 17, 3947–3958.
- Shiau, J., Keawsawasvong S., Yodsomjai, W., 2023. Determination of support pressure for the design of square box culverts. *Int. J. Geomech.*, 23 (1), 06022035
- Shiau, J., Keawsawasvong S., Banyong, R., 2023. Terzaghi's three stability factors for pipeline burst-related ground stability. *J. Pipeline Science and Eng.*, 3 (4), 100128
- Sloan, S.W., 2013. Geotechnical stability analysis. *Geotechnique*, 63(7), 531-72.
- Stanglin, D. (n.d.). "This was a major, a major break": Houston schools, businesses closed after pipe bursts, causing flooding. USA TODAY. <https://www.usatoday.com/story/news/nation/2020/02/28/houston-water-main-break-flooding-boil-advisory/4901547002/>. (Accessed 31 Dec. 2020).

- www.abc.net.au. (2010). *Burst water main leaves crater, flood damage*. <https://www.abc.net.au/news/2010-08-25/burst-water-main-leaves-crater-flood-damage/957306>. (Accessed 31 Dec. 2020).
- www.abc.net.au. (2020). *Moment Perth sinkhole swallows front half of car caught on camera*. <https://www.abc.net.au/news/2020-07-10/caught-on-video-sinkhole-swallows-part-of-car-in-perth/12442252>.
- Xu, M., Cao, Y., Ni, P., and Mei, G., 2020. Infiltration analysis of perforated storm sewer: finite difference modelling versus field tests. *J. Hydrol.* 590, 125421.
- Zhang, F., Gao, Y.F., Wu, Y.X., and Zhang, N., 2018. Upper-bound solutions for face stability of circular tunnels in undrained clays. *Geotechnique*, 68(1), 76-85.
- Zhang, D. M., Du, W. W., Peng, M. Z., Feng, S. J., and Li, Z. L., 2020. Experimental and numerical study of internal erosion around submerged defective pipe. *Tunn. Undergr. Space Technol.*, 97, 103256.



**Dr. Tan Nguyen** received his PhD from Kyoto University, Japan, specializing in geotechnical engineering. His research encompasses computational geomechanics, soil plasticity, numerical methods, and smart computing in civil engineering. As head of the Smart Computing in Civil Engineering Research Group (SCCE) at Ton Duc Thang University (TDTU), Dr. Tan focuses on coupling robust computational methods with smart computing to address a wide range of problems in civil engineering, with a commitment to bridging theory and practical applications in infrastructure development.

**Declaration of interests**

The authors declare that they have no known competing financial interests or personal relationships that could have appeared to influence the work reported in this paper.

The authors declare the following financial interests/personal relationships which may be considered as potential competing interests:

Journal Pre-proof